


Failed supernova simulations beyond black hole formation

Takami Kuroda  ¹★ and Masaru Shibata ^{1,2}

¹Max-Planck-Institut für Gravitationsphysik, Am Mühlenberg 1, D-14476 Potsdam-Golm, Germany

²Center for Gravitational Physics and Quantum Information, Yukawa Institute for Theoretical Physics, Kyoto University, Kyoto 606-8502, Japan

Accepted 2023 September 3. Received 2023 August 31; in original form 2023 July 13

ABSTRACT

We present an axisymmetric failed supernova simulation beyond black hole formation, for the first time with numerical relativity and two-moment multi-energy neutrino transport. To ensure stable numerical evolution, we use an excision method for neutrino radiation hydrodynamics within the inner part of black hole domain. We demonstrate that our excision method is capable of stably evolving the radiation hydrodynamics in dynamical black hole space–time. As a remarkable signature of the final moment of proto-neutron star (PNS), we find the emergence of high-energy neutrinos. Those high-energy neutrinos are associated with the PNS shock surface being swallowed by the central black hole and could be a possible observable of failed supernovae.

Key words: gravitational waves – neutrinos – stars: black holes – supernovae: general.

1 INTRODUCTION

Massive stellar collapse is one of the main formation channels of stellar-mass black hole (BH), whose existence was observationally substantiated through numerous coalescence events (e.g. Abbott et al. 2016, 2019). Massive stars heavier than $\sim 8 M_{\odot}$ undergo a catastrophic gravitational core collapse (CC) at the end stage of their evolution. The subsequent evolutionary path is rich in variety and determines the remnant property. Broadly speaking, less to moderately massive stars explode as core-collapse supernova (CCSN), whereas more massive stars are prone to fail the explosion, sometimes completely and sometimes exhibiting only a feeble explosion (Nomoto et al. 2006; Tanaka et al. 2009). At the same time, some of more massive stars are known to be accompanied by a very energetic explosion termed as hypernova (Iwamoto et al. 1998), whose explosion energy is about one order of magnitude larger than those of canonical supernovae (SNe).

The CCSN explosion scenario and the mass range determining the fate are yet to be fully understood (for reviews, see Janka, Melson & Summa 2016; Müller 2016; Burrows & Vartanyan 2021). It is evident, however, that unless the explosion possesses sufficient energy to expel substantial amounts of stellar mantle, the central compact remnant will ultimately acquire a mass that surpasses the maximum mass limit, above which its internal pressure cannot counteract its own self-gravitational force, thereby leading to the formation of a black hole. The remnant property is tightly connected with its progenitor mass (Woosley, Heger & Weaver 2002; Heger et al. 2003). In general, the more massive the progenitor, the higher the probability of being BH. Moreover, recent parametric studies, focusing on the explodability by the standard neutrino heating mechanism, have revealed that the compactness (O’Connor & Ott 2011) could potentially be a good indicator of BH formation (see also e.g. Ugliano et al. 2012; Ertl et al. 2016; Müller et al. 2016;

Sukhbold et al. 2016; Ebinger et al. 2019). Like these, the formation of a BH is predominantly determined by the compactness of the progenitor star, along with the detailed explosion scenario (but see Burrows & Vartanyan 2021 for counterexamples).

There are currently numerous multidimensional simulations reporting a successful SN explosion (e.g. Burrows et al. 2020; Müller & Varma 2020; Stockinger et al. 2020; Bollig et al. 2021; Nakamura, Takiwaki & Kotake 2022; Vartanyan, Coleman & Burrows 2022). These studies are primarily directed towards less massive, or more precisely less compact, progenitor stars, in which the canonical neutrino heating mechanism can trigger the explosion, leaving behind a neutron star (NS). However, there are several observational evidences of a ‘failed’ SN (Kochanek et al. 2008; Smartt 2015; Adams et al. 2017). These events report a sudden disappearance of red supergiant, inferring that the whole progenitor star collapses and becomes a BH without noticeable explosions. Furthermore, exceptionally low-energy SNe, e.g. SN 2008ha (Foley et al. 2009; Valenti et al. 2009), were detected, which could possibly be explained by ‘fallback’ during SN explosion (Fryer et al. 2009; Kawabata et al. 2010). Should these events be a gravitational collapse of massive star, the remnant becomes most likely a BH due to their inferred small ejecta mass.

These observations associated possibly with a BH formation strongly motivate us to explore the failed and fallback SN scenarios. There were, however, severe numerical difficulties in performing SN simulations in BH space–time. First, multidimensional SN simulations in general relativity (GR), for instance with numerical relativity, are still minor, e.g. Müller, Janka & Dimmelmeier (2010) (and its subsequent works) using the so-called conformal flatness condition (CFC) or Kuroda, Takiwaki & Kotake (2016) with a Baumgarte–Shapiro–Shibata–Nakamura (BSSN) formalism (Shibata & Nakamura 1995; Baumgarte & Shapiro 1999). Since BHs are fundamentally general relativistic objects, the formation process, namely from the onset of gravitational collapse of massive progenitor to BH formation and beyond, can be precisely followed only by numerical relativity. Secondly, sophisticated neutrino transport is

* E-mail: takami.kuroda@aei.mpg.de

essential for modern SN simulations. However, numerical relativity simulation in BH space–time combined with sophisticated neutrino transport is currently still challenging. To date, simulations only up to BH formation (Kuroda et al. 2018; Shibagaki et al. 2020; Kuroda et al. 2022) or switching to Newtonian gravity with a large excision region (several times of the Schwarzschild radius) immediately after BH formation (Chan et al. 2018; Rahman et al. 2022) are reported. Very recently, Sykes et al. (2023) reported the first SN simulations solving the full spatial domain above the BH, i.e. without discarding too large computational domain in the vicinity of central BH, based on the CFC metric.

The main obstacle of neutrino transport in BH space–time, or rather immediately after BH formation, stems from the rapid change of matter field. At the moment of BH formation, the (rest-mass) density just above the BH is generally high, $\gtrsim 10^{14} \text{ g cm}^{-3}$. The density, however, quickly decreases to $\sim 10^{10} \text{ g cm}^{-3}$ within a few ms concomitantly with the proto-neutron star (PNS) being swallowed by the central BH. This indicates that the region in the vicinity of the BH rapidly shifts from optically thick to thin condition and such extreme condition makes neutrino transport with full interactions a significantly challenging subject. In addition, the matter (and probably also radiation) field inside the BH is typically required to be ‘excised’ for stable numerical evolution. As of now, however, there is no concrete method how we should treat the radiation field inside the excised region and also inside BH for stable numerical evolution.

In this study, we report our first SN simulation beyond BH formation with numerical relativity and multi-energy neutrino transport. We use an excision method for both matter and neutrino radiation fields inside a part of BH domain. Our excision method demonstrates stable evolution immediately after BH formation as well as in the subsequent BH accretion phase. Furthermore, we find the emergence of high-energy neutrinos associated with the PNS shock surface being swallowed by the central BH, which could potentially be a probe of the very final moment of PNS. We also show that these high-energy neutrinos could be detectable by the current and next-generation neutrino detectors if the BH formation happens in our Galaxy.

This paper is organized as follows. Section 2 starts with a concise summary of our GR radiation hydrodynamic scheme with an excision scheme and also describe the initial set-up of the simulation. The main results and detailed analysis of our new findings are presented in Section 3. We summarize our results and conclude in Section 4. Throughout the paper, Greek indices run from 0 to 3 and Latin indices from 1 to 3, except ν and ε , which denote neutrino species and energy, respectively.

2 METHOD

In our full GR radiation hydrodynamic simulations, we solve the evolution equations of metric, hydrodynamics, and energy-dependent neutrino radiation. Each of the evolution equations is solved in an operator-splitting manner, while the system evolves self-consistently as a whole, satisfying the Hamiltonian and momentum constraints (Kuroda et al. 2016). In Section 2.1, we describe our numerical method focusing particularly on the excision method applied to the neutrino radiation hydrodynamic variables. Section 2.2 is devoted to explaining the computed model and numerical set-up.

2.1 Radiation hydrodynamics in BH space–time

We solve full GR multi-energy neutrino transport equations in axisymmetric $2 + 1$ dimensions (two spatial dimensions and one

momentum-space dimension). Details of the code are described in our previous studies (Kuroda et al. 2016, 2022). The black hole space–time is evolved using the BSSN formalism (Shibata & Nakamura 1995; Baumgarte & Shapiro 1999) with a fourth-order finite differencing for the spatial derivatives and a four-step Runge–Kutta method. We choose ‘ $1 + \log$ ’ slicing condition for the lapse and gamma-driver condition for the shift vector (Alcubierre et al. 2003). BH formation is determined by identifying the location of apparent horizon (AH) by an AH finder, e.g. Shibata (1997). After the AH formation, we enforce an excision method for radiation hydrodynamics inside the AH, while we evolve the full black hole space–time without excision for geometrical variables.

Here, we will briefly explain our excision technique for radiation hydrodynamics. Once the AH is found, we divide the interior of AH into two: inner and outer regions. The interface of these two regions is located at $fr_{\text{AH}}(\theta)$, where $f \in [0, 1]$ and $r_{\text{AH}}(\theta)$ denotes the radius of AH in the θ direction, θ being the angle with respect to z -axis. In the outer region, we solve the full neutrino radiation hydrodynamics in the same way as the outside of AH (i.e. $r > r_{\text{AH}}$). On the other hand, we excise the inner region and artificially set all primitive variables, i.e. the rest-mass density ρ , entropy s , electron fraction Y_e , spacial components of four-velocity u^i , and the zeroth- and first-order neutrino radiation moments ($E_{(\nu,\varepsilon)}, F_{(\nu,\varepsilon)}^i$), as

$$\begin{bmatrix} \rho \\ u^i \\ s \\ Y_e \\ E_{(\nu,\varepsilon)} \\ F_{(\nu,\varepsilon)}^i \end{bmatrix} = \begin{bmatrix} \sim 0.1\rho_{\text{max}} \\ 0 \\ \approx 1.5k_{\text{B}} \text{ baryon}^{-1} \\ \approx 0.15 \\ E_{\text{thick}(\nu,\varepsilon)} \\ F_{\text{thick}(\nu,\varepsilon)}^i \end{bmatrix}, \quad \text{for } r(\theta) \leq fr_{\text{AH}}(\theta). \quad (1)$$

Here, ρ_{max} represents the maximum rest-mass density outside of the AH, which therefore changes its value with time due to the mass accretion on to BH. Regarding the entropy and electron fraction, we use fixed values taken from typical NS structures. The zeroth- and first-order radiation moments ($E_{\text{thick}(\nu,\varepsilon)}, F_{\text{thick}(\nu,\varepsilon)}^i$) inside the inner region are enforced to be the moments in the optically thick limit (cf. equations 6.14–6.15 in Shibata et al. 2011) assuming the beta equilibrium with matter.

We shortly touch the appropriate value for f . Usually, source terms for neutrino–matter interactions including gravitational redshift and Doppler terms are quite *stiff*. Inside the inner region $r(\theta) \leq fr_{\text{AH}}(\theta)$, we do not evolve any radiation–matter fields; that is, these stiff source terms are suddenly switched off across the excision boundary. Such artificial treatment inevitably causes spurious behaviours appearing especially in the radiation fields near the excision boundary. If we choose the value of f to be close to unity, those spurious oscillations eventually propagate even out to the outside of AH and the simulation will be crashed. Therefore, in this study, we set $f = 0.5$ to avoid such pathological behaviour. With these treatments, we found numerically stable neutrino radiation hydrodynamic evolution in BH space–time.

2.2 Model

We use a non-rotating massive star with zero metallicity, whose initial mass at its zero-age main sequence is $70 M_{\odot}$ (Takahashi, Umeda & Yoshida 2014). It has a substantially high compactness parameter $\xi_{2.5} = 1$ (O’Connor & Ott 2011) at the final evolution phase. This progenitor star was reported to form a BH within a few hundred milliseconds after the first bounce (Kuroda et al. 2018; Shibagaki et al. 2021). We use the DD2 EOS of Typel et al. (2010). The maximum NS mass of DD2 for cold and non-rotating case is $2.42 M_{\odot}$, which is consistent with the existence of observationally confirmed

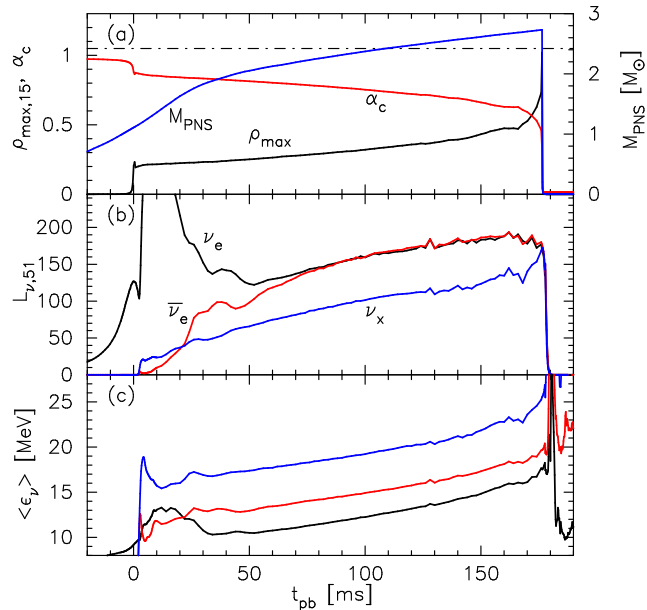


Figure 1. Overall evolution feature. (a) The maximum rest-mass density ρ_{\max} (black), central lapse function α_c (red), and baryon mass of PNS M_{PNS} (blue); (b) neutrino luminosity $L_{\nu,51}$ in units of $10^{51} \text{ erg s}^{-1}$; and (c) neutrino mean energy $\langle \epsilon_\nu \rangle$. Neutrino profiles are evaluated at $r = 400 \text{ km}$. In panels (b) and (c), the colour represents neutrino species: electron-type neutrino (black), electron-type antineutrino (red), and heavy lepton-type neutrino (blue).

massive NSs with $\sim 2 M_\odot$ (Demorest et al. 2010; Antoniadis et al. 2013; Cromartie et al. 2020).

The 2D axially symmetric computational domain extends to $1.5 \times 10^4 \text{ km}$ from the centre. In the cylindrical computational domain, 2:1 ratio nested boxes with 11 refinement levels are embedded, and each nested box contains 64×64 cells so that the finest resolution at the centre becomes $\approx 230 \text{ m}$. In this work, we assume the plane symmetry with respect to the equatorial plane. The neutrino energy space ϵ logarithmically covers from 3 to 400 MeV with 14 energy bins. In this study, we use the up-to-date neutrino rates of Kotake et al. (2018), which are used also in our recent studies (Kuroda et al. 2022; Kuroda & Shibata 2023).

3 RESULTS

We first describe the picture of post-bounce evolution till the formation of BH. Fig. 1 shows the following: (a) the maximum rest-mass density $\rho_{\max,15}$ in units of $10^{15} \text{ g cm}^{-3}$ (black), baryon mass of PNS M_{PNS} (blue), and central lapse function α_c (red); (b) neutrino luminosity $L_{\nu,51}$ in units of $10^{51} \text{ erg s}^{-1}$ for neutrino species; and (c) neutrino mean energy $\langle \epsilon_\nu \rangle$. The PNS surface is defined by the location for which the rest-mass density drops below $10^{10} \text{ g cm}^{-3}$. L_ν and $\langle \epsilon_\nu \rangle$ are evaluated from the emergent neutrino spectra measured at $r = 400 \text{ km}$. In panel (a), we also plot the maximum mass of DD2 EOS for cold and non-rotating stars by the horizontal dash-dotted line of $2.42 M_\odot$.

Panel (a) exhibits that the M_{PNS} exceeds the maximum allowed mass of current EOS at $t_{\text{pb}} \sim 100 \text{ ms}$. However, because of an additional contribution from thermal pressure, the PNS does not immediately collapse to a black hole. From the maximum density evolution, we see a sharp increase at $t_{\text{pb}} \sim 177 \text{ ms}$, at the same time α_c decreases to ~ 0 . This signals the BH formation. Prior to the BH formation at $t_{\text{pb}} \gtrsim 160 \text{ ms}$, electron and anti-electron-type neutrino

luminosities show a decreasing trend, while heavy-lepton neutrinos show a rapid increase in both its luminosity and mean energy. These features were previously identified in 1D full-GR simulations with Boltzmann neutrino transport Liebendörfer et al. (2004) and are commonly observed in the literature, due to rapid contraction of the PNS to the forming BH [see also Sumiyoshi, Yamada & Suzuki (2007), Fischer et al. (2009), Hempel et al. (2012), and Gullin et al. (2022) as well as 3D models by Kuroda et al. (2018) and Shibagaki et al. (2021)]. The overall features before the BH formation are in a good agreement with our former model z70 reported in Kuroda et al. (2022), in which the DD2-based nuclear EOS taking into account a first-order quantum chromodynamics (QCD) phase transition was used. Taking into account the fact that the QCD phase transition occurs after the PNS starts collapsing (Kuroda et al. 2022), the agreement between the current and previous models is quite reasonable.

We also compare BH formation time with previous related studies. O’Connor & Ott (2011) presented a nice correlation between BH formation time, obtained from various 1D GR models, and compactness parameter of progenitor star. According to their fig. 6, massive stars having $\xi_{2.5} = 1$, which is the case for the current model, are forming BH at $t_{\text{pb}} \sim 250\text{--}750 \text{ ms}$, where the time variation reflects the different nuclear EOS. Powell, Müller & Heger (2021) performed faint SN simulations in 3D using a zero-metallicity progenitor star with $85 M_\odot$, whose compactness parameter is $\xi_{2.5} = 0.86$. They witnessed shock revival prior to BH formation, which to some extent suppresses subsequent mass accretions onto the PNS and may delay the BH formation. Their models exhibited BH formation occurring at $t_{\text{pb}} \sim 290\text{--}590 \text{ ms}$. Using similar massive progenitor stars, Rahman et al. (2022) also demonstrated faint SN scenarios with BH formation occurring at $t_{\text{pb}} \sim 350\text{--}400 \text{ ms}$. In addition, a recent study of Sykes et al. (2023) presented BH formation at $t_{\text{pb}} \sim 220 \text{ ms}$ for the same progenitor model used in Powell et al. (2021). Considering that our numerical formalism is totally independent from these previous studies and also that we use a different progenitor model, some time variations in BH formation time are expected to emerge. At the same time, comparing to less massive stars, e.g. with $\xi_{2.5} \sim 0.25$, which are predicted to form BH at $t_{\text{pb}} \gtrsim 2 \text{ s}$ (O’Connor & Ott 2011), unless successful shock revival does not occur, all previous studies including this study are presenting consistent BH formation time, i.e. substantially quicker than $t_{\text{pb}} \gtrsim 2 \text{ s}$ expected in less massive stars.

Next, we discuss the neutrino radiation hydrodynamic evolution after the BH formation, focusing mainly on how effectively our excision method manage to prevent propagation of spurious behaviours often appeared at the excision boundary. Fig. 2 displays spherically averaged spatial profiles of the rest-mass density (top-left), electron fraction (top-right), entropy (middle-left), radial component of the three velocity (middle-right), electron-type neutrino luminosity (bottom-left), and anti-electron-type (solid-line) and heavy lepton-type (dash-dotted line) neutrino luminosities (bottom-right), at several time slices. In the middle-left panel, we supplementary plot a temperature profile, but only at the formation of BH (red dash-dotted line), which is used in the later discussion with Fig. 3. Each colour represents the post BH formation time t_{BH} , denoted in the top-left panel. Once the AH is formed, we plot structures only outside the AH.

Slightly before AH formation at $t_{\text{BH}} = -0.1 \text{ ms}$, the central density exceeds $10^{15} \text{ g cm}^{-3}$ and the velocity profile inside the PNS shows the infalling structure. For $t_{\text{BH}} \geq 0 \text{ ms}$, for which we apply an excision method described in the previous section, we see essentially no numerical instabilities at the interface of the AH. All the neutrino radiation fields and hydrodynamical variables exhibit

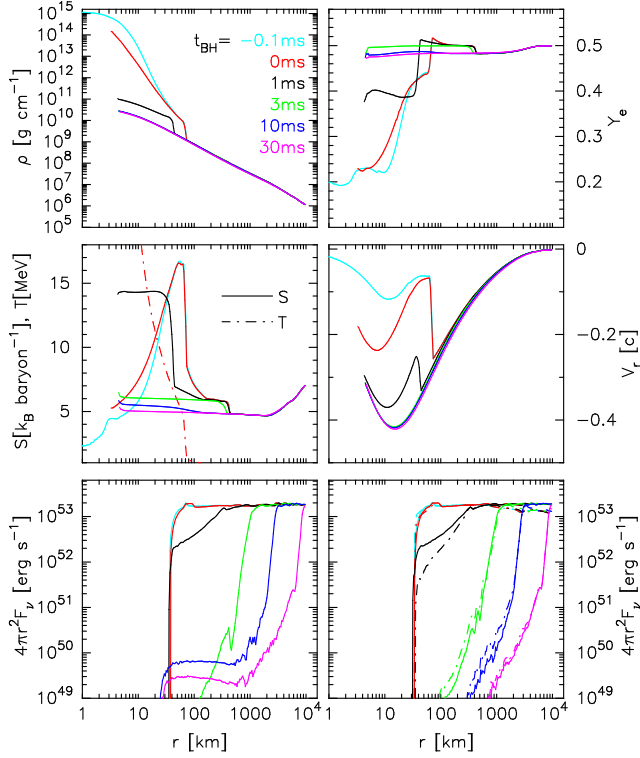


Figure 2. Spherically averaged radial profiles of the rest-mass density ρ (top-left), electron fraction Y_e (top-right), entropy per baryon s (middle-left), radial component of the three-velocity $v^r \equiv u^r/u^t$ (middle-right), neutrino luminosity for ν_e (bottom-left), $\bar{\nu}_e$ (solid, bottom-right), and ν_x (solid-dashed, bottom-right) at different times denoted in the top-left panel. In the middle-left panel, we also plot a temperature profile, but only at $t_{\text{BH}} = 0$ ms (red dash-dotted line).

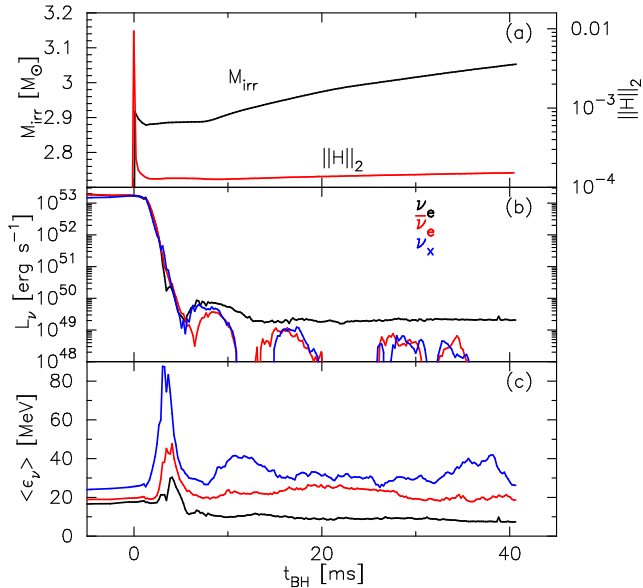


Figure 3. Post BH formation evolution of (a) the irreducible mass M_{irr} and 2-norm of Hamiltonian constraint violation $\|H\|_2$, (b) neutrino luminosities, and (c) mean neutrino energies, as a function of t_{BH} . In panels (b) and (c), the colour represents neutrino species: electron-type neutrino (black), electron-type antineutrino (red), and heavy lepton-type neutrino (blue).

smooth structures across the AH and subsequently swallowed into its inside. From the density structural evolution, the maximum density drops by four orders of magnitude, from $\sim 10^{14}$ to $\sim 10^{10}$ g cm^{-3} , within a few ms, presenting a clear transition from optically thick to thin conditions. This feature makes SN simulations in dynamical BH space-time one of numerically challenging subjects. We found that, if we suddenly switch off the neutrino–matter interactions inside the AH, it causes spurious behaviours, which eventually leak out to the outside and lead to a code crash. Therefore, we believe that it is essential to ensure a buffer zone between the AH and the excised region, especially when the neutrino radiation fields are taken into account. During the first few ms after AH formation, low- Y_e and high-entropy material, which represent typical PNS shocked material, are still present outside the AH. They are, however, immediately swallowed by the BH and for $t_{\text{BH}} \gtrsim 3$ ms the BH accretion enters a nearly steady state, exhibiting high- Y_e (~ 0.49) and relatively low-entropy ($\sim 5 k_B \text{ baryon}^{-1}$) flows (see magenta lines).

Next, we focus on how the neutrino signals in association with the BH formation are radiated away. Bottom two panels indicate that all neutrino species have an outgoing flux for $r \gtrsim 30$ km at the time of the BH formation. In the vicinity of AH, on the other hand, neutrino radiation fields experience a strong drag by infalling high density component ($\gtrsim 10^{12}$ g cm^{-3}) and have an inward flux. After the mass accretion becomes a nearly steady state flow for $t_{\text{BH}} \gtrsim 3$ ms, the dominant neutrino–matter interaction is the electron capture due to continuous replenishment of high- Y_e materials (~ 0.49 , see top-right panel) from stellar mantle. It results in a sustained neutrino emission even after the BH formation for electron-type neutrinos (see blue and magenta lines in the bottom-left panel in Fig. 2), while the rest of neutrino species has essentially no production channel and their neutrino luminosities quickly subside. Sykes et al. (2023) reported a BH excision scheme with neutrino transport. According to their long time failed CCSN simulation in 1D spherical symmetry, qualitatively similar spatial profiles of neutrino luminosities, namely relatively strong ν_e emission continuing even after BH formation, was also reported.

Fig. 3 displays (a) the irreducible mass M_{irr} and 2-norm of Hamiltonian constraint violation $\|H\|_2$, (b) neutrino luminosities, and (c) mean neutrino energies, as a function of t_{BH} . Here, M_{irr} is defined by the area of AH A as $M_{\text{irr}} = \sqrt{A/16\pi}$ (cf. Baumgarte et al. 1996; Shibata 1997) and $\|H\|_2$ measures the constraint violation only for numerical cells outside the AH. From panel (a), the irreducible mass shows an increasing trend from $M_{\text{irr}} \sim 2.88$ to $\sim 3.06 M_\odot$ during the first 40 ms. At the moment of the AH formation, the measured value of the protoneutron star mass, M_{PNS} , is $\sim 2.76 M_\odot$, which rapidly decreases to $\lesssim 0.001 M_\odot$ (the total mass outside of the AH and where $\rho \geq 10^{10}$ g cm^{-3} is met) within a few ms. It means that the estimated M_{irr} is slightly larger than M_{PNS} at $t_{\text{BH}} = 0$ ms. Furthermore, from panel (a), M_{irr} initially shows a slightly odd behaviour, a nearly constant evolution until $t_{\text{BH}} \sim 8$ ms, and it increases afterward. From these, we naively suspect that the current numerical resolution at the centre $\Delta x \sim 230$ m might not be high enough¹ to accurately resolve the location of AH and may tend to overestimate the initial BH mass approximately by $\sim 0.1 M_\odot$, i.e. ~ 3 per cent error in the evaluation for the total BH mass or the AH radius. However, once the system relaxes to a quasi-steady state for $t_{\text{BH}} \gtrsim 10$ ms, M_{irr} increases with a reasonable growth rate of $M_{\text{irr}} \approx 4.66 M_\odot \text{ s}^{-1}$, which agrees approximately with that of the PNS mass, $\dot{M}_{\text{PNS}} \approx 4.73 M_\odot \text{ s}^{-1}$,

¹The BH is resolved by ~ 13 – 14 grid points at its formation.

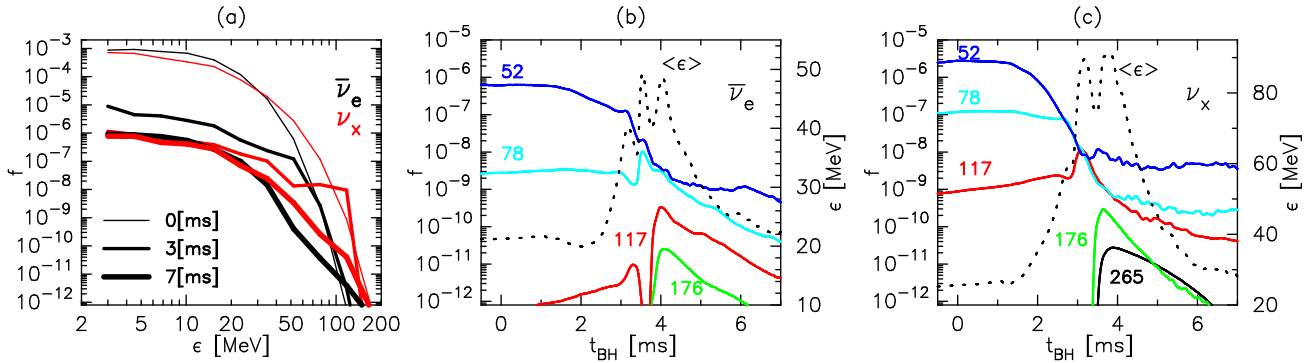


Figure 4. (a) The distribution function f_ε for $\bar{\nu}_e$ (black lines) and ν_x (red lines) at three different time slices: $t_{\text{BH}} = 0$ ms, 3 ms (corresponding to the time when high-energy neutrinos are observed), and 7 ms, (b) time evolution of distribution function f_ε for all energy bins higher than $\varepsilon \geq 52$ MeV (this time, 52, 78, 117, 176, and 265 MeV) (solid lines) and mean energy $\langle \varepsilon \rangle$ (dashed line) for $\bar{\nu}_e$, and (c) same as the panel (b) but for ν_x . All these values are measured at $r = 400$ km.

before the BH formation (see Fig. 1a). The 2-norm of Hamiltonian constraint $\|H\|_2$ stays around $\sim 10^{-4}$ without any secular increase after BH formation.

Regarding the neutrino signals, the neutrino luminosity for all species show a rapid distinction and eventually migrate to a quasi steady state for $t_{\text{BH}} \gtrsim 5$ ms. From panel (b), L_{ν_e} stays around $\sim 2 \times 10^{49}$ erg s^{-1} till the end of our calculation, which features a long-term steady state mass accretion on to the BH. Nearly constant L_{ν_e} of the order of $\mathcal{O}(10^{49})$ erg s^{-1} is also reported in Sykes et al. (2023).

The neutrino mean energy $\langle \varepsilon_\nu \rangle$ may reveal the final moment of devastating PNS collapse. As can be clearly seen, $\langle \varepsilon_\nu \rangle$ for all neutrino species show a drastic increase at $t_{\text{BH}} \sim 3$ ms. This is particularly the case for heavy lepton-type neutrinos, which show a remarkably high mean energy of $\langle \varepsilon_{\nu_x} \rangle \sim 90$ MeV. These values are even higher than those from the QCD CCSN models (Fischer et al. 2018; Kuroda et al. 2022), which are also known to emit high-energy neutrinos $\langle \varepsilon_{\nu_x} \rangle \sim 40$ MeV due to strong shock heating in association with the quark core bounce. We will now shortly discuss their possible excitation mechanism. First, since we measure the emergent neutrino signals at $r = 400$ km, these high-energy neutrinos are produced at $t_{\text{BH}} \sim 1$ –2 ms. From Fig. 2, this time corresponds exactly to the time when huge amounts of hot PNS envelope together with a shock surface infall with a relativistic speed of $\sim 0.3c$. The highest temperature of collapsing PNS material (middle-left panel in Fig. 2) for the regions of $r \gtrsim 30$ km, where F_{ν_x} has a positive sign (bottom-right panel) and can contribute to the emergent neutrino spectrum, is merely $T \sim 10$ MeV. It indicates that heavy lepton-type neutrinos, whose energy are $\langle \varepsilon_{\nu_x} \rangle \sim 30$ MeV, could be barely explained via such a pair production channel, although it is not likely for much higher neutrino energy of ~ 90 MeV.

To further discuss their origin, we examine their spectral features. Fig. 4 depicts (a) the distribution function f_ε^2 for $\bar{\nu}_e$ (black lines) and ν_x (red lines) at three different time slices: $t_{\text{BH}} = 0$ ms, 3 ms (corresponding to the time when high-energy neutrinos are observed), and 7 ms, (b) time evolution of distribution function f_ε

for all energy bins higher than $\varepsilon \geq 52$ MeV (this time, 52, 78, 117, 176, and 265 MeV) (solid lines) and mean energy $\langle \varepsilon \rangle$ (dashed line) for $\bar{\nu}_e$, and (c) same as the panel (b) but for ν_x . All these values are measured at $r = 400$ km.

From panel (a), the energy spectrum at $t_{\text{BH}} = 3$ ms for ν_x exhibits a flatter profile with relatively more populations for neutrinos with $\gtrsim 50$ MeV. Such feature cannot be seen in other two time snapshots. We attribute the flatter profile to a consequence of more effective isoenergy scatterings taking place in the upstream to the relativistically infalling shock surface. Because of the rapid infall of the PNS shock surface (see ν_r -profiles from $t_{\text{BH}} = -0.1$ to 1 ms in Fig. 2), the outgoing comoving neutrino flux ahead of the shock becomes relatively larger. Consequently, the effect of isoenergy neutrino scatterings becomes more prominent compared to the case with a stationary shock surface. Furthermore, that impact is more visible for high-energy neutrinos as the cross-section of the isoenergy scatterings is proportional to the square of the incoming neutrino energy. Indeed, from panel (c), the distribution function for heavy lepton-type neutrinos shows an increase (decreasing) trend for $\varepsilon \geq 117$ (≤ 78) MeV at $t_{\text{BH}} \lesssim 3$ ms. Particularly at the energy bin $\varepsilon = 117$ MeV ($f_{\varepsilon=117}$: red line), its increase is noteworthy with its maximum appearing at $t_{\text{BH}} \sim 3$ ms. Neutrinos at higher energy bins ($\varepsilon = 176$ and 265 MeV) also show a sudden increase with slight time delays of ~ 0.5 ms from the peak time for $f_{\varepsilon=117}$. These time delays are mostly due to that higher energy neutrinos require a longer time for escaping from collapsing stellar mantle. On the other hand, regarding $\bar{\nu}_e$ (as well as ν_e), the less population of high-energy neutrinos ($\varepsilon \gtrsim 50$ MeV) prior to the BH formation than that of ν_x [compare two thin lines in panel (a)] leads simply to a less noticeable increase at $t_{\text{BH}} \sim 3$ –4 ms. Additionally, the presence of charged current reactions tend to suppress their increase. In fact, $f_{\varepsilon \geq 117}$ for $\bar{\nu}_e$ shows approximately an order of magnitude smaller values than that for ν_x . These features result in the observed high-energy neutrinos pronounced for heavy lepton-type ones (Fig. 3). Although our moment formalism cannot capture the particle acceleration mechanisms at the shock front, non-thermal shock acceleration (Kazanas & Ellison 1981; Giovanoni, Ellison & Bruenn 1989; Nagakura & Hotokezaka 2021) is also reported to excite high-energy neutrinos from CCSNe.

As a comparison with previous studies, Gullin et al. (2022) has performed a GR Monte Carlo neutrino transport and reported high-energy neutrinos with $\langle \varepsilon_{\nu_x} \rangle \sim 50$ MeV in association with BH formation. Since their calculations are performed on the fixed space-time and matter fields after BH formation, quantitative differences

²We reconstruct the distribution function f_ε simply by $f_\varepsilon = J_\varepsilon / 4\pi \varepsilon^3$, where J_ε denotes the zeroth-order neutrino radiation moment measured in the comoving frame at the energy bin ε . With an appropriate closure relation, J_ε is determined from the zeroth- and first-order radiation momenta ($E_\varepsilon, F_\varepsilon^\mu$), which are measured in the Eulerian frame and are the basic variables evolved in our M1 neutrino transport.

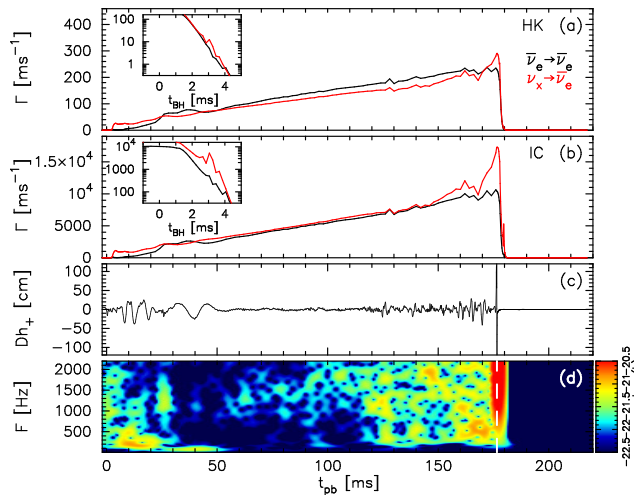


Figure 5. (a) The neutrino detection rate Γ of HK; (b) Γ of IC; (c) matter origin gravitational waves Dh_+ ; and (d) spectrogram of h_+ obtained by a short-time Fourier transform. We assume a source distance of $D = 10$ kpc.

in $\langle \varepsilon_\nu \rangle$ from ours are inevitable. We, however, believe that the emission of high-energy neutrinos just after the BH formation seem to be a common feature and might be used as a smoking gun of infall of PNS surface. Rahman et al. (2022) performed CCSN simulations with BH formation. However, since they excise the innermost 400 km once they find the AH and also their models present a successful shock expansion, i.e. corresponding to the fallback SN model, the emergence of high-energy neutrinos similar to ours was not reported.

Finally, we discuss observable multimessenger signals for a current failed CCSN model. Fig. 5 displays from top (a) the neutrino detection rate Γ of Hyper-Kamiokande (HK) (Abe et al. 2011; Hyper-Kamiokande Proto-Collaboration 2018); (b) Γ of IceCube (IC) (Abbasi et al. 2011; Salathe, Ribordy & Demirörs 2012); (c) matter origin gravitational waves (GWs) Dh_+ ; and (d) spectrogram of h_+ obtained by a short-time Fourier transform. We assume a source distance of $D = 10$ kpc. h_+ is the gravitational wave strain, which is calculated from a standard quadrupole formula, and we show only the non-vanishing component in axisymmetric profile observed along the equatorial plane. The neutrino detection rate Γ is evaluated in the same way as Kuroda et al. (2022) assuming a Fermi–Dirac distribution for the neutrino energy spectrum (Lund et al. 2010; Takiwaki & Kotake 2018). Note that in the evaluation for Γ , we consider two extreme cases: all $\bar{\nu}_e$ emitted from the source reach the detectors without neutrino flavour conversion and cause the signal at the detectors (black lines in the figure); all $\bar{\nu}_x$ (identical to ν_x in this study) emitted from the source are completely swapped by $\bar{\nu}_e$ and cause the signals (red lines). In inset of the upper two panels, we show a magnified view of Γ relative to BH formation time t_{BH} to feature detection of high-energy neutrinos.

Regarding the neutrino detection rate Γ , both of the two extreme cases, i.e. with and without neutrino flavour conversion, essentially show a quantitatively similar monotonic increase until the BH formation. This feature can be seen for both detectors. This indicates that the possible range of neutrino oscillation effects (see Mirizzi et al. 2016, for a review), i.e. the region bounded by two lines in panels (a) and (b), is quite small, compared to previous studies using less massive progenitor stars (e.g. Tamborra et al. 2012; Kuroda et al. 2022). For instance, $\Gamma_{\bar{\nu}_e \rightarrow \bar{\nu}_e}$ becomes ~ 1.5 times higher than $\Gamma_{\bar{\nu}_x \rightarrow \bar{\nu}_e}$ for $t_{\text{pb}} \gtrsim 100$ ms for CCSN models with less massive progenitor stars, while the current one with a more massive progenitor star

presents roughly comparable values. Another remarkable feature is rapid increase of $\Gamma_{\bar{\nu}_x \rightarrow \bar{\nu}_e}$ (red lines) as the PNS approaches BH formation ($t_{\text{pb}} \gtrsim 150$ ms). It is a clear signature of the increasing behaviour of both L_{ν_x} and $\langle \varepsilon_{\nu_x} \rangle$ shown in Fig. 1. We also discuss whether the high-energy heavy lepton-type neutrinos, as a possible signature of the shock surface being swallowed by BH, could be observed. From insets, we can marginally observe a slight increase for $\Gamma_{\bar{\nu}_x \rightarrow \bar{\nu}_e}$ (red lines) at $t_{\text{BH}} \sim 3$ ms, which is more visible for IC. This time is consistent with the emission time of high-energy neutrinos (see Fig. 3c). If we could observe such a tentative increase of neutrino detection during the exponential decay, it could be a possible signature of the aforementioned final moment of the PNS shock surface.

Bottom two panels show the emitted GWs. We see essentially the same features as have been discussed for model z70 in Kuroda et al. (2022). During the first ~ 50 ms after bounce, relatively large and low-frequency GWs originated from post-bounce convective motions are observed, whose amplitudes and frequencies reach ~ 50 cm and ~ 100 Hz, respectively. Afterwards, the gravitational waveform shows a considerable subsidence, which is then disrupted at $t_{\text{pb}} \gtrsim 120$ ms. At the moment of BH formation, burst-like GWs of the order of ~ 100 cm are emitted presenting a broad-band emission. Once the BH is formed and BH accretion settles into a quasi-steady state for $t_{\text{BH}} \gtrsim 3$ ms, we observe essentially no GWs for the current non-rotating model. As a comparison to a previous 2D GR study (Rahman et al. 2022), which performed faint SN simulations using an $80 M_\odot$ progenitor star, the current GWs show consistent behaviours in the initial convection phase ($t_{\text{pb}} \lesssim 50$ ms). During this phase, the amplitude and typical frequency reach $Dh \sim 30\text{--}40$ cm and $F \sim 100$ Hz, respectively, in their non-rotating model. These values are quite consistent with our findings. Although a direct comparison in the subsequent phase ($t_{\text{pb}} \gtrsim 50$ ms till BH formation) may not be so meaningful, as their models are faint SNe, i.e. exhibiting shock revival before BH formation, high-frequency GWs ($F \sim 1000$ Hz) are also observed prior to BH formation, which could potentially be another common feature.

4 SUMMARY

We have presented results of 2D axisymmetric CCSN simulation for a massive star with $70 M_\odot$. Our CCSN model is based on numerical relativity, which solves the GR neutrino radiation hydrodynamic equations together with the two-moment (M1) neutrino transport equations of Kuroda et al. (2016). We used up-to-date neutrino opacities following Kotake et al. (2018) and employed the DD2 EOS of Typel et al. (2010). In this framework, we follow for the first time ‘beyond BH formation’. To ensure stable numerical evolution, we use an excision method for neutrino radiation hydrodynamics, while we evolve the geometrical variables for entire computational domain.

Our results showed consistent PNS evolution and multimessenger signals during the PNS contraction phase with previous studies, for which the same progenitor model was used (Kuroda et al. 2018, 2022; Shibagaki et al. 2021). The current non-rotating PNS model exceeds the maximum NS mass for DD2 EOS at ~ 100 ms after bounce. Subsequently, it initiates the second gravitational collapse, resulting in BH formation at $t_{\text{pb}} \sim 177$ ms. After we identify the AH, our excision technique demonstrates its capability to stably evolve the radiation hydrodynamics in dynamical BH space–time. We solve the full neutrino–matter interactions taking into account the gravitational redshift and Doppler terms from the AH down to the excision domain, so that spurious oscillations often appearing

around the excision surface do not leak outside the AH. We also mention that our current numerical method satisfies the Hamiltonian constraint well and its violation after BH formation is free from secular growth.

After the BH formation, the PNS envelope was simply swallowed by the BH and the system transitions to a nearly steady BH accretion phase within a few ms. Afterwards, the BH mass, i.e. the area of AH, gradually increases because of the continuous mass inflow. The accretion flow is composed of high- Y_e (~ 0.5) material, reflecting the component of progenitor core (i.e. iron).

In contrast, to the simple collapse dynamics of PNS, its impact on the emergent neutrino signals was not so trivial. Our findings are as follows: (1) neutrinos with significantly high energies, especially for heavy lepton-type neutrinos whose mean energy reaches ~ 90 MeV, are observed during the infall phase of PNS envelope and (2) a steady-state neutrino emission of electron-type neutrinos in the BH accretion phase. Possible observations of high-energy neutrinos from BH formation are also reported in a previous similar (but spherical symmetric) study by Gullin et al. (2022). We attribute the first feature to more efficient isoenergy scatterings between neutrinos, which strive to emerge from the shock surface, and infalling stellar mantle ahead of the shock, which is mainly composed of heavy nuclei. Using time evolution of neutrino spectral property, we showed that propagation of high-energy neutrinos is indeed hindered, when the PNS shock surface drastically collapses (i.e. $1 \text{ ms} \lesssim t_{\text{BH}} \lesssim 2 \text{ ms}$). Once the shock surface is engulfed by the BH, those neutrinos are radiated away, with some time delays for higher energy neutrinos. In the BH accretion phase, the main component of accretion flow is high- Y_e stellar mantle, whose temperature is at the highest a few MeV. Therefore, the main neutrino emission channel is the electron capture on heavy nuclei occurring in the vicinity of AH. It results in a nearly constant electron-type neutrino luminosity as also reported in Sykes et al. (2023). We would like to emphasize that these neutrino properties could be revealed only by full neutrino radiation hydrodynamic simulations with numerical relativity without excising the relevant region outside the AH, i.e. by fully solving the region outside the BH.

In this study, we employed only one non-rotating progenitor model. In our future works, we are interested in exploring various CCSN models accompanied by BH formation. For instance, a fallback scenario is one of the interesting topics. The current progenitor model has a significantly high compactness $\xi_{2.5} = 1.0$ at pre-collapse stage (O'Connor & Ott 2011; and see also table 1 in Kuroda et al. 2022), which leads to strong mass accretions during the PNS contraction phase. Therefore, it induces the PNS core collapse without affording an opportunity for shock revival. However, if one considers less compact stars (Chan et al. 2018; Powell et al. 2021) or rotating stars (Rahman et al. 2022), the shock revival aided by neutrino heating could happen before BH formation. Such systems could be observed as a faint SN (Kochanek et al. 2008; Adams et al. 2017) and should be distinguished from the current failed SN (or direct BH formation) model with no shock revival. Progenitor model dependence should definitely be explored in the future study to explain various observations.

Another interesting topic to be explored is the collapsar scenario (MacFadyen & Woosley 1999) as a possible route to long gamma-ray bursts and hypernovae. In the collapsar scenario, a BH surrounded by a massive disc is formed, i.e. highly non-spherical system is formed. Such systems can be followed only in numerical relativity with no approximation like CFC approximation. For instance, after the formation of a massive disc, viscous effects significantly heat the disc, leading eventually to the launch of energetic outflows

(in the context of both NS mergers and massive stellar collapse, see e.g. Fernández & Metzger 2013; Just et al. 2015; Fujibayashi et al. 2020a, b, 2023). As another intriguing and also a challenging topic in the context of collapsar scenario, the impact of magnetic fields threading the central BH is undoubtedly worth to be explored as a possible origin of relativistic jets generated via e.g. the Blandford–Znajek mechanism (Blandford & Znajek 1977). It has been recently demonstrated by Christie et al. (2019) and Hayashi et al. (2022) that the Blandford–Znajek mechanism is a promising mechanism for launching a jet, but only in the framework of compact mergers. We will explore this fascinating topic in our future CCSN studies.

ACKNOWLEDGEMENTS

We acknowledge K. Kiuchi, S. Fujibayashi, and A. Betranhandy for fruitful discussions. This work was in part supported by Grant-in-Aid for Scientific Research (Nos. 20H00158 and 23H04900) of Japanese MEXT/JSPS. Numerical computations were carried out on Sakura and Raven clusters at Max Planck Computing and Data Facility.

DATA AVAILABILITY

The data underlying this article will be shared on reasonable request to the corresponding author.

REFERENCES

- Abbasi R. et al., 2011, *A&A*, 535, A109
 Abbott B. P. et al., 2016, *ApJ*, 818, L22
 Abbott T. M. C. et al., 2019, *ApJ*, 872, L30
 Abe K. et al., 2011, preprint (arXiv:1109.3262)
 Adams S. M., Kochanek C. S., Gerke J. R., Stanek K. Z., Dai X., 2017, *MNRAS*, 468, 4968
 Alcubierre M., Brüggmann B., Diener P., Koppitz M., Pollney D., Seidel E., Takahashi R., 2003, *Phys. Rev. D*, 67, 084023
 Antoniadis J. et al., 2013, *Science*, 340, 448
 Baumgarte T. W., Shapiro S. L., 1999, *Phys. Rev. D*, 59, 024007
 Baumgarte T. W., Cook G. B., Scheel M. A., Shapiro S. L., Teukolsky S. A., 1996, *Phys. Rev. D*, 54, 4849
 Blandford R. D., Znajek R. L., 1977, *MNRAS*, 179, 433
 Bollig R., Yadav N., Kresse D., Janka H.-T., Müller B., Heger A., 2021, *ApJ*, 915, 28
 Burrows A., Vartanyan D., 2021, *Nature*, 589, 29
 Burrows A., Radice D., Vartanyan D., Nagakura H., Skinner M. A., Dolence J. C., 2020, *MNRAS*, 491, 2715
 Chan C., Müller B., Heger A., Pakmor R., Springel V., 2018, *ApJ*, 852, L19
 Christie I. M., Lalakos A., Tchekhovskoy A., Fernández R., Foucart F., Quataert E., Kasen D., 2019, *MNRAS*, 490, 4811
 Cromartie H. T. et al., 2020, *Nat. Astron.*, 4, 72
 Demorest P. B., Pennucci T., Ransom S. M., Roberts M. S. E., Hessels J. W. T., 2010, *Nature*, 467, 1081
 Ebinger K., Curtis S., Fröhlich C., Hempel M., Perego A., Liebendörfer M., Thielemann F.-K., 2019, *ApJ*, 870, 1
 Ertl T., Janka H. T., Woosley S. E., Sukhbold T., Ugliano M., 2016, *ApJ*, 818, 124
 Fernández R., Metzger B. D., 2013, *MNRAS*, 435, 502
 Fischer T., Whitehouse S. C., Mezzacappa A., Thielemann F.-K., Liebendörfer M., 2009, *A&A*, 499, 1
 Fischer T. et al., 2018, *Nat. Astron.*, 2, 980
 Foley R. J. et al., 2009, *AJ*, 138, 376
 Fryer C. L. et al., 2009, *ApJ*, 707, 193
 Fujibayashi S., Shibata M., Wanajo S., Kiuchi K., Kyutoku K., Sekiguchi Y., 2020a, *Phys. Rev. D*, 101, 083029
 Fujibayashi S., Shibata M., Wanajo S., Kiuchi K., Kyutoku K., Sekiguchi Y., 2020b, *Phys. Rev. D*, 102, 123014

- Fujibayashi S., Kiuchi K., Wanajo S., Kyutoku K., Sekiguchi Y., Shibata M., 2023, *ApJ*, 942, 39
- Giovanoni P. M., Ellison D. C., Bruenn S. W., 1989, *ApJ*, 342, 416
- Gullin S., O'Connor E. P., Wang J.-S., Tseng J., 2022, *ApJ*, 926, 212
- Hayashi K., Fujibayashi S., Kiuchi K., Kyutoku K., Sekiguchi Y., Shibata M., 2022, *Phys. Rev. D*, 106, 023008
- Heger A., Fryer C. L., Woosley S. E., Langer N., Hartmann D. H., 2003, *ApJ*, 591, 288
- Hempel M., Fischer T., Schaffner-Bielich J., Liebendörfer M., 2012, *ApJ*, 748, 70
- Hyper-Kamiokande Proto-Collaboration, 2018, *Prog. Theor. Exp. Phys.*, 2018, 063C01
- Iwamoto K. et al., 1998, *Nature*, 395, 672
- Janka H.-T., Melson T., Summa A., 2016, *Annu. Rev. Nucl. Part. Sci.*, 66(1): 341
- Just O., Bauswein A., Ardevol Pulpillo R., Goriely S., Janka H. T., 2015, *MNRAS*, 448, 541
- Kawabata K. S. et al., 2010, *Nature*, 465, 326
- Kazanas D., Ellison D. C., 1981, in International Cosmic Ray Conf., Proc. of the 17th International Cosmic Ray Conf., Paris, p. 176
- Kochanek C. S., Beacom J. F., Kistler M. D., Prieto J. L., Stanek K. Z., Thompson T. A., Yüksel H., 2008, *ApJ*, 684, 1336
- Kotake K., Takiwaki T., Fischer T., Nakamura K., Martínez-Pinedo G., 2018, *ApJ*, 853, 170
- Kuroda T., Shibata M., 2023, *Phys. Rev. D*, 107, 103025
- Kuroda T., Takiwaki T., Kotake K., 2016, *ApJS*, 222, 20
- Kuroda T., Kotake K., Takiwaki T., Thielemann F.-K., 2018, *MNRAS*, 477, L80
- Kuroda T., Fischer T., Takiwaki T., Kotake K., 2022, *ApJ*, 924, 38
- Liebendörfer M., Messer O. E. B., Mezzacappa A., Bruenn S. W., Cardall C. Y., Thielemann F.-K., 2004, *ApJS*, 150, 263
- Lund T., Marek A., Lunardini C., Janka H.-T., Raffelt G., 2010, *Phys. Rev. D*, 82, 063007
- MacFadyen A. I., Woosley S. E., 1999, *ApJ*, 524, 262
- Mirizzi A., Tamborra I., Janka H. T., Saviano N., Scholberg K., Bollig R., Hüdepohl L., Chakraborty S., 2016, *Nuovo Cimento Rivista Serie*, 39, 1
- Müller B., 2016, *PASA*, 33, e048
- Müller B., Varma V., 2020, *MNRAS*, 498, L109
- Müller B., Janka H.-T., Dimmelmeier H., 2010, *ApJS*, 189, 104
- Müller B., Heger A., Liptai D., Cameron J. B., 2016, *MNRAS*, 460, 742
- Nagakura H., Hotokezaka K., 2021, *MNRAS*, 502, 89
- Nakamura K., Takiwaki T., Kotake K., 2022, *MNRAS*, 514, 3941
- Nomoto K., Tominaga N., Umeda H., Kobayashi C., Maeda K., 2006, *Nucl. Phys. A.*, 777, 424
- O'Connor E., Ott C. D., 2011, *ApJ*, 730, 70
- Powell J., Müller B., Heger A., 2021, *MNRAS*, 503, 2108
- Rahman N., Janka H. T., Stockinger G., Woosley S. E., 2022, *MNRAS*, 512, 4503
- Salathe M., Ribordy M., Demirörs L., 2012, *Astropart. Phys.*, 35, 485
- Shibagaki S., Kuroda T., Kotake K., Takiwaki T., 2020, *MNRAS*, 493, L138
- Shibagaki S., Kuroda T., Kotake K., Takiwaki T., 2021, *MNRAS*, 502, 3066
- Shibata M., 1997, *Phys. Rev. D*, 55, 2002
- Shibata M., Nakamura T., 1995, *Phys. Rev. D*, 52, 5428
- Shibata M., Kiuchi K., Sekiguchi Y., Suwa Y., 2011, *Prog. Theor. Phys.*, 125, 1255
- Smartt S. J., 2015, *PASA*, 32, e016
- Stockinger G. et al., 2020, *MNRAS*, 496, 2039
- Sukhbold T., Ertl T., Woosley S. E., Brown J. M., Janka H. T., 2016, *ApJ*, 821, 38
- Sumiyoshi K., Yamada S., Suzuki H., 2007, *ApJ*, 667, 382
- Sykes B., Mueller B., Cordero-Carrión I., Cerdá-Durán P., Novak J., 2023, *Phys. Rev. D*, 107, 103010
- Takahashi K., Umeda H., Yoshida T., 2014, *ApJ*, 794, 40
- Takiwaki T., Kotake K., 2018, *MNRAS*, 475, L91
- Tamborra I., Müller B., Hüdepohl L., Janka H.-T., Raffelt G., 2012, *Phys. Rev. D*, 86, 125031
- Tanaka M. et al., 2009, *ApJ*, 692, 1131
- Typel S., Röpke G., Klähn T., Blaschke D., Wolter H. H., 2010, *Phys. Rev. C*, 81, 015803
- Ugliano M., Janka H.-T., Marek A., Arcones A., 2012, *ApJ*, 757, 69
- Valenti S. et al., 2009, *Nature*, 459, 674
- Vartanyan D., Coleman M. S. B., Burrows A., 2022, *MNRAS*, 510, 4689
- Woosley S. E., Heger A., Weaver T. A., 2002, *Rev. Mod. Phys.*, 74, 1015

This paper has been typeset from a $\text{\TeX}/\text{\LaTeX}$ file prepared by the author.